Contents lists available at ScienceDirect

Applied Catalysis B: Environmental

Symmetry-dependent photocatalysis of conjugated microporous polymers based on pyrene for oxygenation of sulfides with O2

Xia Li [a,b], Yuexin Wang [b], Fulin Zhang [b], Xianjun Lang [b,*]

[a] Ministry of Education Key Laboratory for the Green Preparation and Application of Functional Materials, School of Materials Science and Engineering, Hubei University, Wuhan 430062, China
[b] Sauvage Center for Molecular Sciences, Hubei Key Lab on Organic and Polymeric Optoelectronic Materials, College of Chemistry and Molecular Sciences, Wuhan University, Wuhan 430072, China

ABSTRACT

To date, conjugated microporous polymers (CMPs) have been developed into multifaceted photocatalysts. Here, two CMPs based on pyrene with the linkages of thiazolo[5,4-*d*]thiazole (TzTz) are prepared for visible light photocatalysis. The dimension of the molecular building block's symmetry on the property and activity of CMPs is systematically investigated. Py(4)-TzTz-CMP with a pyrene building block of D_{2h} symmetry gives rise to better optoelectronic property than Py(2)-TzTz-CMP with a pyrene building block of C_2 symmetry. Therefore, Py(4)-TzTz-CMP photocatalyst is endowed with superior conversions for the green light-promoted oxygenation of sulfides with O2. Intriguingly, mechanistic explorations disclose that both superoxide and singlet oxygen are responsible for the production of the target sulfoxides. This work gives insight into the rational design of highly active CMP photocatalysts for selective chemical transformations.

1. Introduction

Increasingly, conjugated microporous polymers (CMPs) have been developed into multifaceted photocatalysts with the extended π-conjugated backbones enabling substantial visible light collection and the inherent porous structures permitting mass transfer [1–6]. Thanks to abundant molecular building blocks and versatile synthetic protocols, various CMPs have been prepared by the flexible combination of electron acceptors and donors [7–10]. Visible light photocatalysis of CMPs, aiming at sustainable solutions, has been capitalized on different applications such as hydrogen production [11–16], carbon dioxide reduction [17–20], and organic pollutant degradation [21–23]. Hence, extensive efforts have been made to pursue state-of-the-art photocatalysts of CMPs by rational molecular design. However, the structure–activity relationship remains elusive for CMPs towards these reactions because the primary reactants and products are complex that interface with the inorganic and the organic. This challenge calls for a more straightforward scheme. In response, CMPs flourish as a versatile photocatalytic platform for a series of organic reactions [24–29]. In such a scenario, the primary reactants and products are organic that could be easily traced to navigate a more accurate picture of the structure–activity relationship of CMPs.

Selective organic transformations over inorganic semiconductor photocatalysts have made considerable advances [30–35], but persist on inadequate visible light harvesting ability and limited charge separation efficiency. In contrast, visible light-promoted selective organic transformations over CMPs at ambient conditions open a pathway towards more efficiently utilizing solar energy [36–39]. To exploit low-energy photons, CMPs witness expansive visible light absorption by adapting the molecular building blocks at various dimensions.

Hitherto, CMPs composed of electron-rich and planar pyrene have implemented visible light-promoted hydrogen production [40], carbon dioxide reduction [41], and selective organic transformations [42–44]. Meanwhile, much attention has been focused on the connections between structure and activity over CMPs based on pyrene. For example, by introducing alkynyl groups, the influence of π-conjugation on the photocatalytic activities of CMPs based on pyrene for selective oxidation reactions was investigated [43]. By incorporating pyrene and dithieno (3,2-b:2′,3′-d)thiophene 4,4-dioxide, CMPs could capture red light for selective oxidation of amines [44]. These reported CMPs, however, were prepared by coupling reactions over Pd-complexes. A minute amount of Pd might be remained in the prepared CMPs which might impact the ultimate activity of photocatalysis. It would be preferable to prepare CMPs without the involvement of a metal catalyst, such as direct

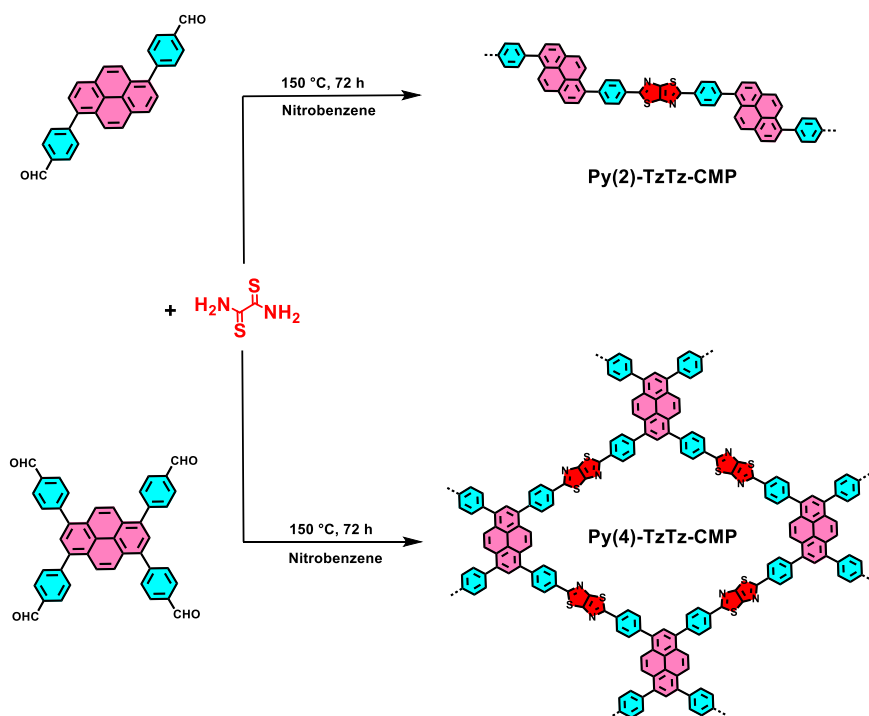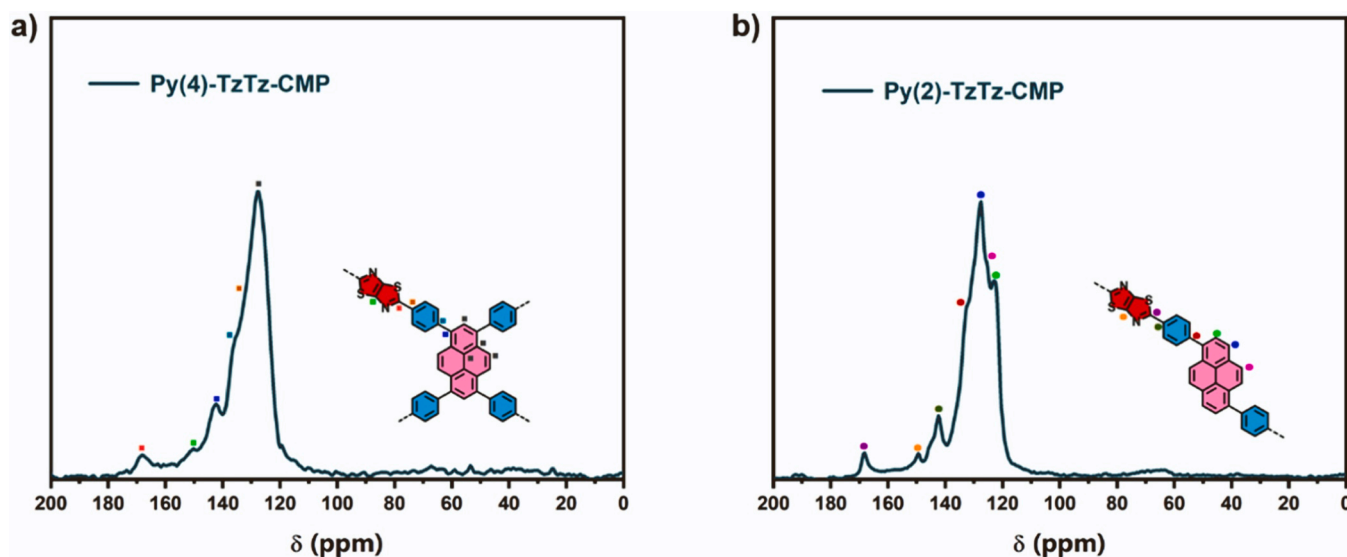**Scheme 1.** The preparations of the two CMPs based on pyrene.

Fig. 1. Solid-state ^{13}C NMR spectra of the two CMPs based on pyrene a) Py(4)-TzTz-CMP and b) Py(2)-TzTz-CMP.

condensations. Considering structural variations of CMPs, however, the dimension of symmetry of the molecular building blocks that affect the porosity, energy band structure, and charge transport of CMPs should be scrutinized to get close to unrivaled photocatalytic activity.

Herein, two CMPs based on pyrene with the linkages of thiazolo[5,4-*d*]thiazole (TzTz) are prepared to carry out the selective oxygenation of sulfides with O_2. In particular, the dimension of the molecular building block's symmetry on the activity is systematically considered. The molecular building block's symmetry directly affects the conjugation of CMPs, significantly impacting their optoelectronic property and subsequent photocatalytic activity. Py(4)-TzTz-CMP prepared with a building block of D_{2h} symmetry gives rise to a better photocatalytic activity than Py(2)-TzTz-CMP constructed with a building block of C_2 symmetry, accounting for faster separation and transport of charge carriers.

Intriguingly, mechanistic explorations affirm that both superoxide ($O_2^{\bullet-}$) and singlet oxygen ($^1O_2$) are reactive oxygen species (ROS) responsible for the formation of sulfoxides. This work gives insight into the rational design of highly active CMP photocatalysts for selective chemical transformations.

2. Experimental section

2.1. Preparations of the two CMPs based on pyrene

The preparations of Py(4)-TzTz-CMP and Py(2)-TzTz-CMP are as follows. Firstly, tetra(4-formylphenyl)pyrene (70.8 mg, 0.114 mmol)/ 4,4′-(pyrene-1,6-diyl)dibenzaldehyde (93.6 mg, 0.228 mmol), dithiooxamide (27.4 mg, 0.228 mmol), nitrobenzene (4 mL) were
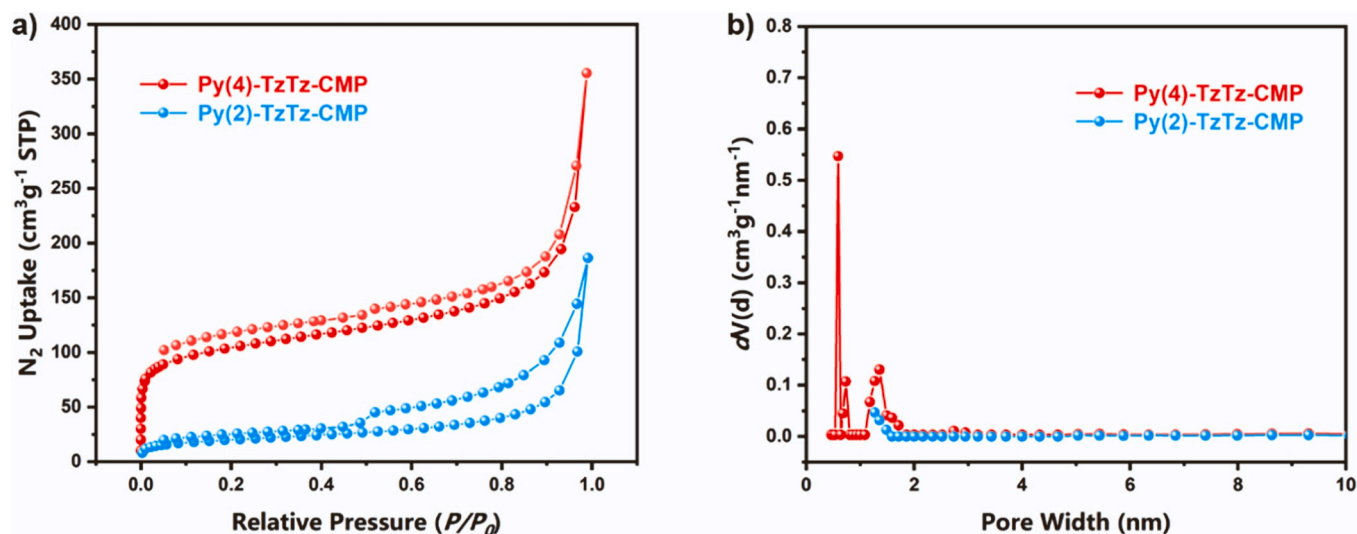
Fig. 2. a) N$_2$ adsorption and desorption isotherms at 77 K and b) pore size distributions of the two CMPs based on pyrene.
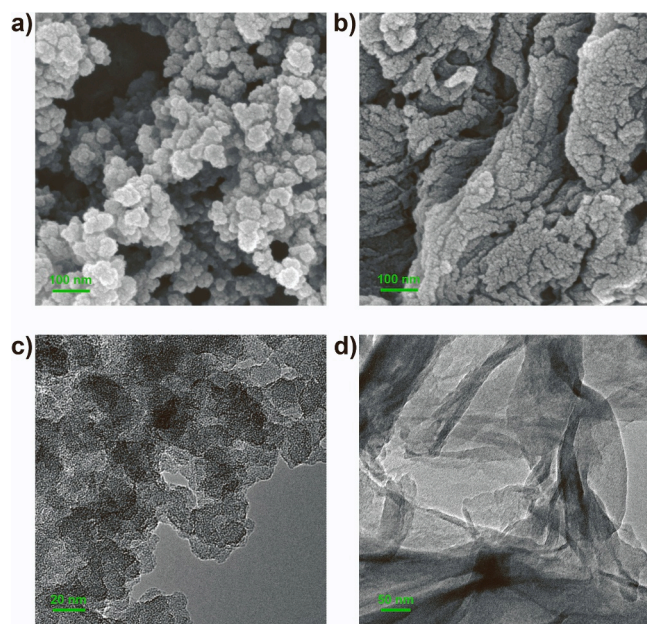

Fig. 3. SEM images of the two CMPs based on pyrene a) Py(4)-TzTz-CMP and b) Py(2)-TzTz-CMP; TEM images of the two CMPs based on pyrene c) Py(4)-TzTz-CMP and d) Py(2)-TzTz-CMP.

charged in a 10 mL Pyrex tube. Secondly, the mixture was homogenously dispersed by 5 min of ultrasonication. Subsequently, the tube with the mixture was flash frozen in the 77 K liquid N$_2$ bath and degassed by three freeze–pump–thaw cycles, which was further flame-sealed in a vacuum and maintained for 72 h at 150 °C. After reaction, the precipitate was collected by filtration and washed successively with dichloromethane and *N,N*-dimethylformamide until the filtrate was transparent. Further, the filter cake was purified with dichloromethane for 72 h in a Soxhlet extractor. The target product was eventually obtained after desiccation under infrared light for 3 h.

2.2. Procedure for the oxygenation of sulfide

First, thioanisole (0.5 mmol), CMP (5 mg), and CH$_3$OH (1 mL) were put into a 10 mL Pyrex reactor. The sealed reactor was injected with 0.1 MPa O$_2$ after stirring for 30 min in the dark to achieve

adsorption–desorption equilibrium. At room temperature, the Pyrex reactor was then irradiated by green LEDs (light-emitting diodes) and stirred at 1500 rpm simultaneously. The pressured O$_2$ was released and the photocatalyst was removed after reaction. Ultimately, in the supernatant, the products were identified by gas chromatography–mass spectrometry (GC–MS). The quantitative analysis of the products using an internal standard method was operated by gas chromatography with flame ionization detection (GC–FID).

3. Results and discussion

3.1. Preparation and characterizations of the two CMPs based on pyrene

In Scheme 1, the preparations of Py(4)-TzTz-CMP and Py(2)-TzTz-CMP are displayed. In essence, 1,3,6,8-tetra(4-formylphenyl)pyrene, a D_{2h} building block, was employed to condensate with dithiooxamide to give Py(4)-TzTz-CMP. In comparison, 4,4′-(pyrene-1,6-diyl)dibenzaldehyde, a C_2 building block, was used to react with dithiooxamide to prepare Py(2)-TzTz-CMP. Both CMPs were prepared via a catalyst-free solvothermal method. Notably, in the preparation process, the solvent of nitrobenzene was also the proton and electron acceptor for the formation of the two CMPs. The obtained brown-yellow powders were insoluble in the tested common solvents. Subsequently, Fourier transform infrared (FTIR) spectroscopy was utilized to verify the creation of TzTz rings in CMPs. In the FTIR spectra of Py(4)-TzTz-CMP and Py(2)-TzTz-CMP (Supplementary Fig. S1), the signal peak appearing at 1635 cm^{-1} belongs to the stretching vibration of the C═N bond, while the signal peak located at 836 cm^{-1} corresponds to the stretching vibration of the C–S–C bond of thiazole rings, which implies TzTz structure was successfully constructed in the targeted CMPs. More detailed information on their chemical structures is further revealed in the solid-state ^{13}C nuclear magnetic resonance (NMR) spectra (Fig. 1). Both CMPs exhibited a signal peak at 168 ppm, arising from the carbon atom of C═N in the formed TzTz linkage. It was also observed the chemical shift at 150 ppm originated from the other sp^2 carbon in the TzTz rings. Moreover, the signal peak ascribed to the aromatic carbon next to TzTz was detected at 134 ppm for Py(4)-TzTz-CMP and 140 ppm for Py(2)-TzTz-CMP. A clear broad peak attributed to the rest of aromatic carbons was also found at 128 ppm.

Next, the permanent porosities of the two CMPs based on pyrene were examined by N$_2$ sorption isotherms at 77 K. Based on Brunauer−Emmett−Teller (BET) model, the specific surface areas of Py(4)-TzTz-CMP and Py(2)-TzTz-CMP were reckoned to be 335 and 69 m^2 g^{-1}, respectively. The N$_2$ adsorption and desorption curves of Py(4)-TzTz-
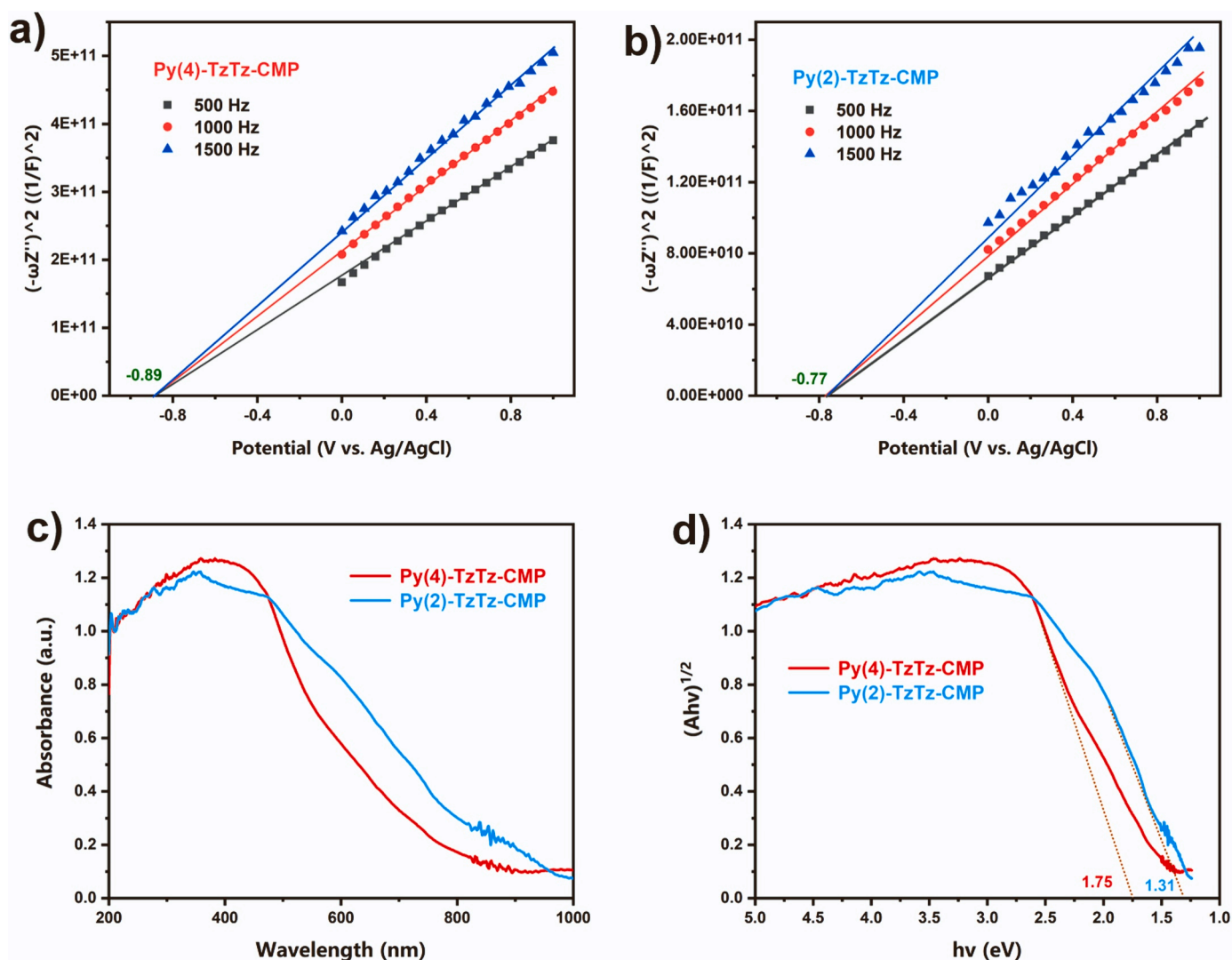
Fig. 4. a) Mott–Schottky plots of Py(4)-TzTz-CMP; b) Mott–Schottky plots of Py(2)-TzTz-CMP; c) UV–Vis DRS of the two CMPs based on pyrene; d) Tauc plots of the two CMPs based on pyrene.

CMP in Fig. 2a are in line with typical type I isotherm that performed sharp N₂ uptake at low relative pressure, indicative of the existence of microporous. In contrast, Py(2)-TzTz-CMP exhibited the characteristic type IV isotherm with the trifling increase for the N₂ uptake at low relative pressure and the appearance of a hysteresis loop in the sorption curves, hinting the existence of mesopores or macropores. Further, the pore size distributions were obtained based on the quenched solid density functional theory (DFT) model. As presented in Fig. 2b, the average pore width of Py(4)-TzTz-CMP is less than 2 nm, further proving its microporous structure. Nevertheless, the pore size distribution of Py (2)-TzTz-CMP indicated very few pore structures, suggesting the building block's symmetry straightly affects the porosity and the BET specific surface areas of CMPs.

Next, the amorphous feature of Py(4)-TzTz-CMP was exposed by the broad pattern in the powder X-ray diffraction (PXRD) patterns. In contrast, several diffraction peaks emerged in the PXRD pattern of Py (2)-TzTz-CMP, which might be triggered by the π–π stacking interaction (Supplementary Fig. S2). Subsequently, the morphologies of the two CMPs based on pyrene were inspected by electron microscopy. The scanning electron microscopy (SEM) image indicates Py(4)-TzTz-CMP was composed of a large number of flake nanoparticles with notable aggregation, thus holding abundant hole structures (Fig. 3a). But an irregular stacking lamellar conglomerate morphology was observed

from the SEM image of Py(2)-TzTz-CMP (Fig. 3b). Correspondingly, atomic force microscopy (AFM) images (Supplementary Fig. S3) reveal the average thickness was 1.43 nm for Py(4)-TzTz-CMP and 12.61 nm for Py(2)-TzTz-CMP. Next, the morphologies of the two CMPs were checked by transmission electron microscopy (TEM) (Fig. 3, c and d), conforming to their SEM images. In addition, the thermal stability of the two CMPs based on pyrene was also investigated by thermal gravimetric analysis (TGA). The TGA curves show that both CMPs had high temperatures of thermal decomposition. The two CMPs based on pyrene withstood temperatures up to 300 and 400 °C, respectively (Supplementary Fig. S4).

It is well established that energy level structure directly influences the light-harvesting ability and redox potentials of a semiconductor photocatalyst. Thus, the energy levels and bandgaps were investigated systematically by Mott–Schottky tests and ultraviolet–visible diffuse reflectance spectroscopy (UV–Vis DRS). Firstly, the Mott–Schottky curves tested at three different frequencies of 500, 1000, and 1500 Hz displayed positive slopes for Py(4)-TzTz-CMP and Py(2)-TzTz-CMP, unveiling that both CMPs are typical n-type semiconductors. Generally, the lowest unoccupied molecular orbital (LUMO) level is close to the flat band potential for an n-type semiconductor, which could be acquired from the Mott–Schottky curves. Therefore, the LUMO levels of the two CMPs were estimated to be −0.89 and −0.77 V versus Ag/AgCl,
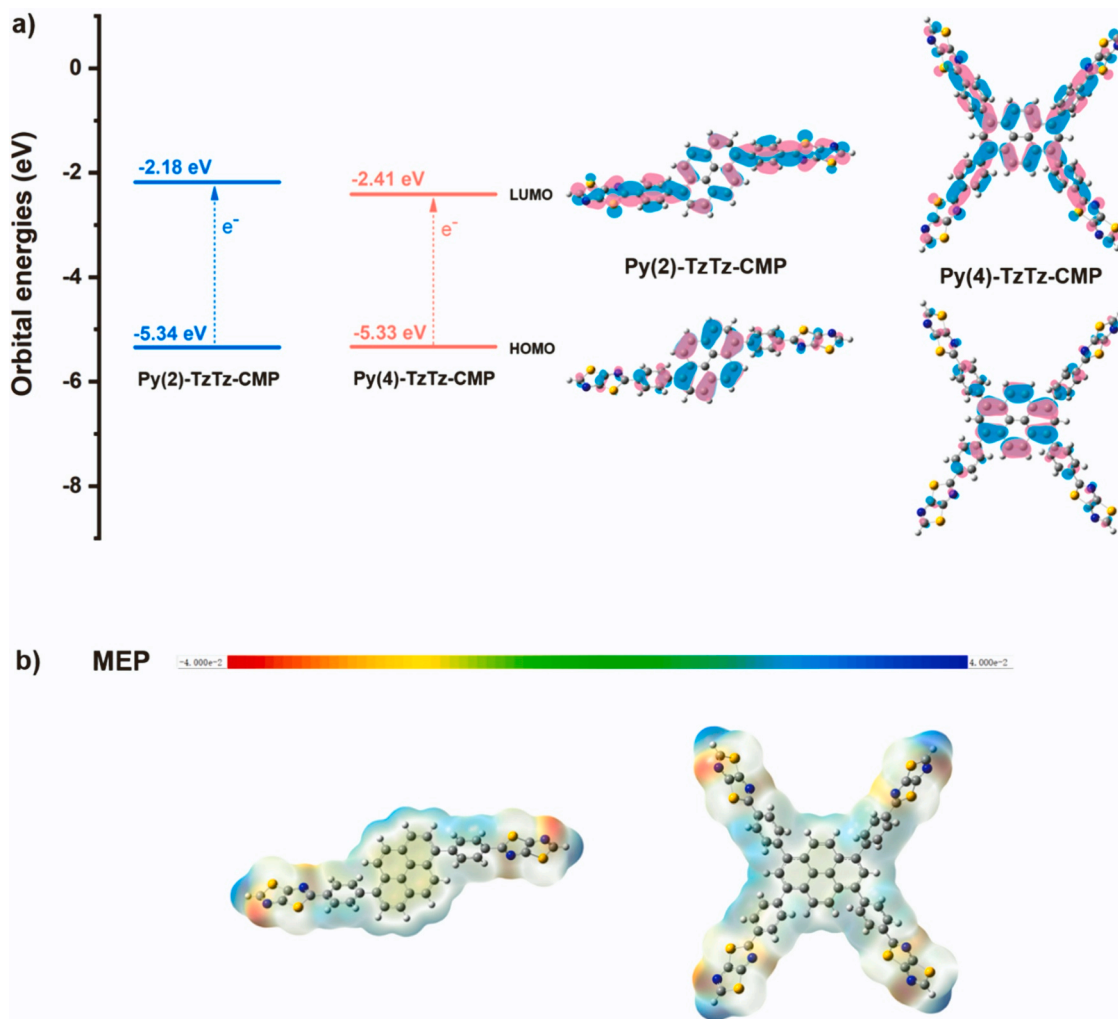
Fig. 5. a) The calculated frontier molecular orbital energy levels and wave function distributions, and b) MEPs for the optimized fragment structures of the two CMPs based on pyrene.
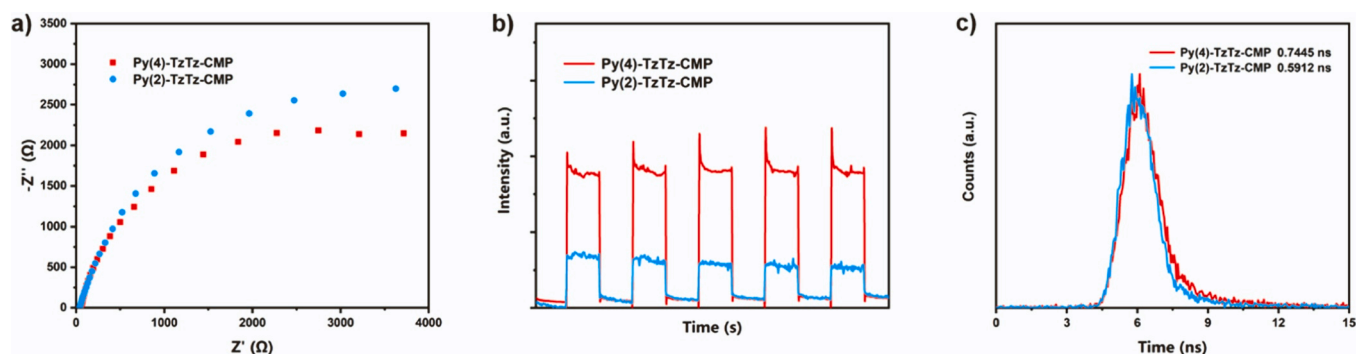

Fig. 6. a) EIS, b) transient photocurrent, and c) TRPL spectra of the two CMPs based on pyrene.

respectively (Fig. 4, a and b). Intrinsically, both CMPs are capable of activating O_2 to $O_2^{\bullet-}$, because their LUMO potential levels are more negative than the reduction potential of $O_2/O_2^{\bullet-}$ (-0.48 V versus Ag/AgCl). Furthermore, the wide optical response ranges measured by UV–Vis DRS indicated that both CMPs have excellent visible light absorption capability (Fig. 4c). The optical bandgaps of Py(4)-TzTz-CMP and Py(2)-TzTz-CMP were assessed as 1.75 and 1.31 eV, respectively, according to the Kubelka–Munk equation (Fig. 4d). The narrower bandgap of Py(2)-TzTz-CMP might be ascribed from its tighter stacking

structure. Based on the LUMO levels and optical bandgaps, the highest occupied molecular orbital (HOMO) levels of Py(4)-TzTz-CMP and Py(2)-TzTz-CMP were calculated as $+0.86$ and $+0.54$ V versus Ag/AgCl, respectively.

To get more sight of the electronic structure of the two CMPs based on pyrene, theoretical DFT calculations at the B3LYP/6–31 G(d,p) level were operated with the optimized fragment structures. The theoretical LUMO and HOMO energy levels, as well as the frontier orbital wave function distributions, are displayed in Fig. 5a. For eliminating the
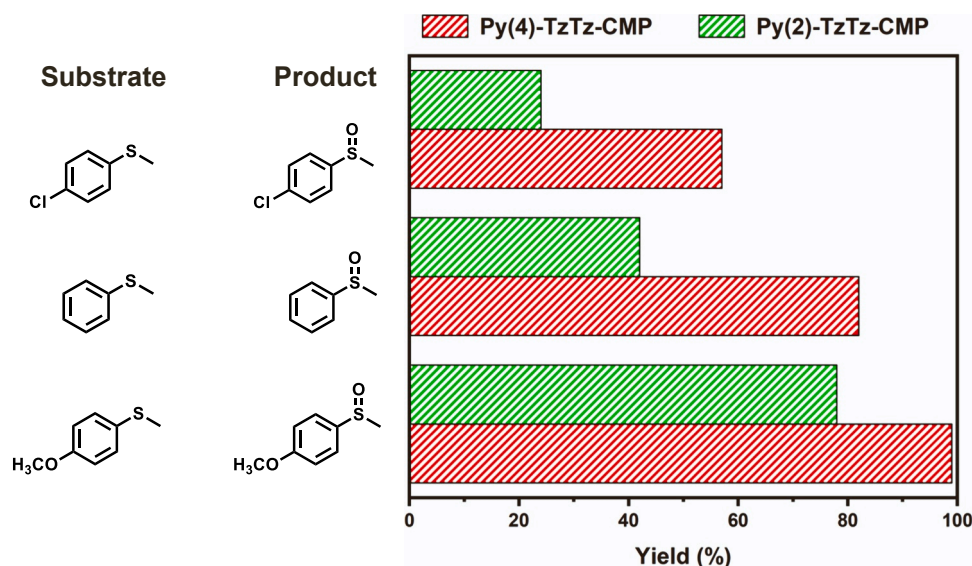
Fig. 7. Comparison of the two CMP photocatalysts for the green light-promoted oxygenation of sulfides. Reaction conditions: sulfide (0.5 mmol), CMP (5 mg), green LEDs ($\lambda = 520 \pm 15$ nm, 3 W × 4), O_2 (0.1 MPa), CH_3OH (1 mL), 1.85 h.

interference of the stacking effect, the calculated bandgap of the optimized fragment structures of Py(4)-TzTz-CMP (2.92 eV) was smaller than that of Py(2)-TzTz-CMP (3.16 eV). Notwithstanding, both are much larger than the optical bandgaps measured by UV–Vis DRS. Intriguingly, the charge density distribution of HOMO and LUMO orbitals for the optimized fragment structures of Py(4)-TzTz-CMP and Py(2)-TzTz-CMP indicated that the HOMO is centered on the pyrene unit while the LUMO is evenly dispersed along the conjugated backbone, illuminating the facile intramolecular electron transfer from the pyrene segment to the TzTz ring under light irradiation. Moreover, the molecular electrostatic potentials (MEPs) in Fig. 5b reveal that negative potential chiefly locates on the N atom of the TzTz ring, and the difference in electrostatic potential distributions of the two CMPs are mainly attributed to the symmetry of their building block.

After determining the energy levels of the two CMPs based on pyrene, the optoelectronic property were further checked by electrochemical impedance spectroscopy (EIS), transient photocurrent tests, and time-resolved photoluminescence (TRPL) spectra. Compared with Py(2)-TzTz-CMP, Py(4)-TzTz-CMP exhibited a smaller semicircle diameter in the Nyquist plot detected by EIS, revealing faster charge mobility. Also, Py(4)-TzTz-CMP displayed a much stronger photocurrent response (Fig. 6c), suggesting its higher efficiency of photogenerated charge separation and migration. Moreover, the charge separation of the two CMPs was also characterized by time-resolved photoluminescence (TRPL) spectra. Markedly, the results indicate that the average fluorescence lifetime of Py(4)-TzTz-CMP was longer than that of Py(2)-TzTz-CMP. Convincingly, the superior separation and transfer of photogenerated charge carriers of Py(4)-TzTz-CMP were further demonstrated by the linear sweep voltammetry (LSV) curves and surface photovoltage (SPV) spectra (Supplementary Fig. S5).
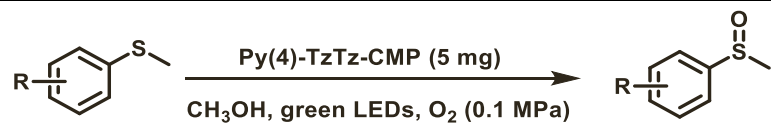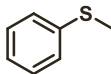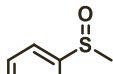
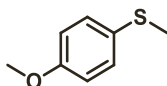### 3.2. Photocatalytic oxygenation of sulfides
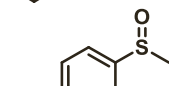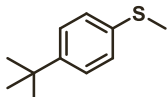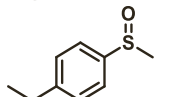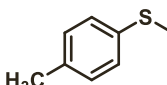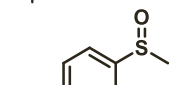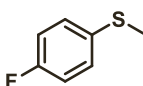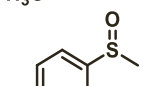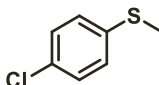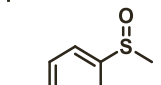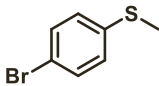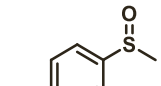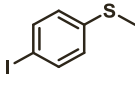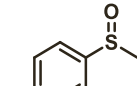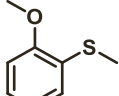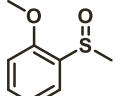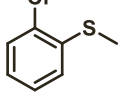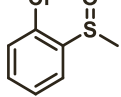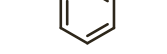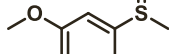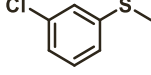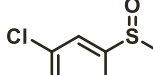
Selective oxygenation of organic sulfides comes to light as a model reaction to properly establish the structure–property relationship of vastly different photocatalysts [45–52]. Due to the electron-rich and planar structure of pyrene [53], both Py(4)-TzTz-CMP and Py (2)-TzTz-CMP possess suitable redox positions, remarkable optoelectronic property, and high chemical and thermal stability, thus green light-promoted selective oxygenation of sulfides with O_2 was implemented to evaluate the photocatalytic activity. As shown in Fig. 7, both CMPs could selectively convert thioanisole to methyl phenyl sulfoxide

with O_2. However, the Py(4)-TzTz-CMP prepared with a D_{2h} building block delivered a superior photocatalytic activity than the Py (2)-TzTz-CMP constructed with a C_2 building block, and 82% conversion of thioanisole was obtained within 1.85 h, much higher than that of Py(2)-TzTz-CMP (42%), which might be ascribed to a much faster separation and transport efficiency of photogenerated charge carriers. In addition, control experiments were also performed under the irradiation of blue LEDs, and the results indicated that the photocatalytic activity of Py(4)-TzTz-CMP is superior to that of Py(2)-TzTz-CMP, which exhibited a much higher conversion (73%) of thioanisole than that of Py (2)-TzTz-CMP (13%). Subsequently, the generality of this discovery was further demonstrated by employing thioanisoles with a *para*-substituted electron-donating group (CH_3O–) or electron-withdrawing group (Cl–) as the substrates. Next, the time course of the green light-promoted selective oxidation reaction was observed to get more insights (Supplementary Fig. S6). It was found that both the kinetic curves conform to the characteristics of zero-order reaction and superior photocatalytic activity could be achieved by Py(4)-TzTz-CMP at each period, suggesting the rational selection of the symmetry of the building blocks is important for designing a highly active CMP photocatalyst.

Furthermore, the photocatalytic activity of Py(4)-TzTz-CMP in different visible regions was examined by using LEDs with varying peak wavelengths (λ_p) as the light sources (Supplementary Table S1). Gratifyingly, blue LEDs could promote the oxygenation of thioanisole with O_2 by Py(4)-TzTz-CMP photocatalysis with the highest conversion, corresponding to its UV–Vis DRS. For a better exploitation of low-energy photons, green light was selected to promote the oxygena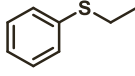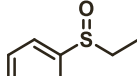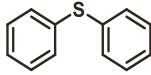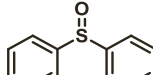tion of thioanisole with O_2. Besides, the impact of light intensity on photocatalytic activity was also investigated (Supplementary Table S2). The oxygenation of thioanisole did not proceed in the dark and the conversions of thioanisole coincided well with the increase of light intensity, highlighting the vital role of light in the oxidation reaction. In addition, the conversions of thioanisole also increased with increasing the amount of photocatalyst Py(4)-TzTz-CMP (Supplementary Table S3).

To further certify the general applicability of Py(4)-TzTz-CMP photocatalyst towards the selective oxygenation of sulfides with O_2, a range of organic sulfides were chosen as substrates. Irradiated by green LEDs, all the thioanisole derivatives equipped with diverse functional groups displayed in Table 1 could be converted into the targeted sulfoxides over Py(4)-TzTz-CMP under an atmosphere of O_2 with high conversions (>90%) and selectivities (>90%) (Table 1, entries 1–13). Nevertheless, their reaction rates were changed with the variation of functional groups

Table 1
Green light-promoted selective oxygenation of sulfides with O_2 by Py(4)-TzTz-CMP photocatalysis[a].

Entry	Substrate	Product	t (h)	Conv. (%)[b]	Sel. (%)[b]
1			2.1	90	98
2			1.8	97	97
3			1.9	99	98
4			1.5	98	97
5			2.2	91	98
6			2.8	90	97
7			2.9	91	98
8			3	95	98
9			2	98	98
10			4.5	90	97
11			2.2	90	98
12			4.3	97	98
13			3	97	88
14			3.1	11	98

(continued on next page)

Table 1 (*continued*)

Entry	Substrate	Product	t (h)	Conv. (%)[b]	Sel. (%)[b]
15	2-naphthyl methyl sulfide	2-naphthyl methyl sulfoxide	4.5	73	94
16	thiane	thiane S-oxide	2.1	99	98
17	*n*-Bu–S–*n*-Bu	*n*-Bu–S(O)–*n*-Bu	2.1	99	97

Reaction scheme (top of table):

R–C6H4–S–CH3 →[Py(4)-TzTz-CMP (5 mg); CH3OH, green LEDs, O2 (0.1 MPa)] R–C6H4–S(O)–CH3

[a] Reaction conditions: Py(4)-TzTz-CMP (5 mg), sulfide (0.5 mmol), O_2 (0.1 MPa), green LEDs (520 ± 10 nm, 3 W × 4), CH_3OH (1 mL).

[b] Determined by GC–FID using chlorobenzene as the internal standard, conversion of sulfide, and selectivity of sulfoxide.
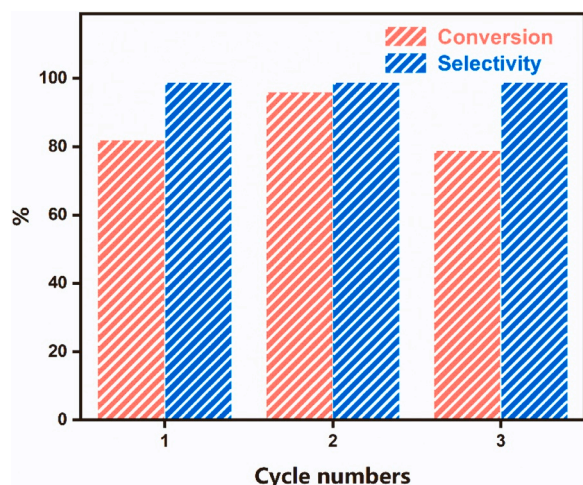
Fig. 8. Py(4)-TzTz-CMP recycling tests for the green light-promoted oxygenation of thioanisole with O_2.

in the aromatic ring. In contrast to thioanisole, the reaction rates of sulfides with electron-donating groups were faster. They followed the order of *p*-CH$_3$ > *p*-OCH$_3$ > *p*-C(CH$_3$)$_3$ > *p*-H (Table 1, entries 1–4), while the reaction rates of sulfides with electron-withdrawing groups were slower and subjected to the order of *p*-I < *p*-Br < *p*-Cl < *p*-F (Table 1, entries 5–8). Besides, the location of substituted groups also influenced the activity of Py(4)-TzTz-CMP. To achieve comparable conversions, the reaction time for the oxygenation of sulfides with −Cl substituted groups increased from *para* to *meta* to *ortho* (Table 1, entries 6, 10, and 12). In contrast, the reaction time for the oxygenation of sulfides with a *para*-substituted −OCH$_3$ group adhered to the *meta* < *ortho* < *para* order (Table 1, entries 2, 9, and 11). However, not all sulfides could be transformed smoothly in the photocatalytic process. When the methyl group of thioanisole was replaced by an ethyl group, a decline in selectivity was observed (Table 1, entry 13). Due to the prominent steric impact, diphenyl sulfide and 2-naphthyl sulfide were converted sluggishly (Table 1, entries 14 and 15). Encouragingly, the smooth conversions of aliphatic sulfides to the corresponding sulfoxides were achieved with desired selectivities (Table 1, entries 16 and 17). Moreover, after being subjected to three recycling tests for the oxygenation of thioanisole with O_2, there was no apparent decline in the activity for Py(4)-TzTz-CMP photocatalyst (Fig. 8). Subsequently, the recyclability of the photocatalyst was further proved through

Fig. 9. a) ROS quenching experiments; b) The influence of O_2 pressure on the oxygenation of thioanisole.

Fig. 10. The recorded EPR spectra: a) The e^- of Py(4)-TzTz-CMP; b) DMPO trapped $O_2^{\bullet-}$ and c) TMPD trapped $^1O_2$ during Py(4)-TzTz-CMP photocatalysis.
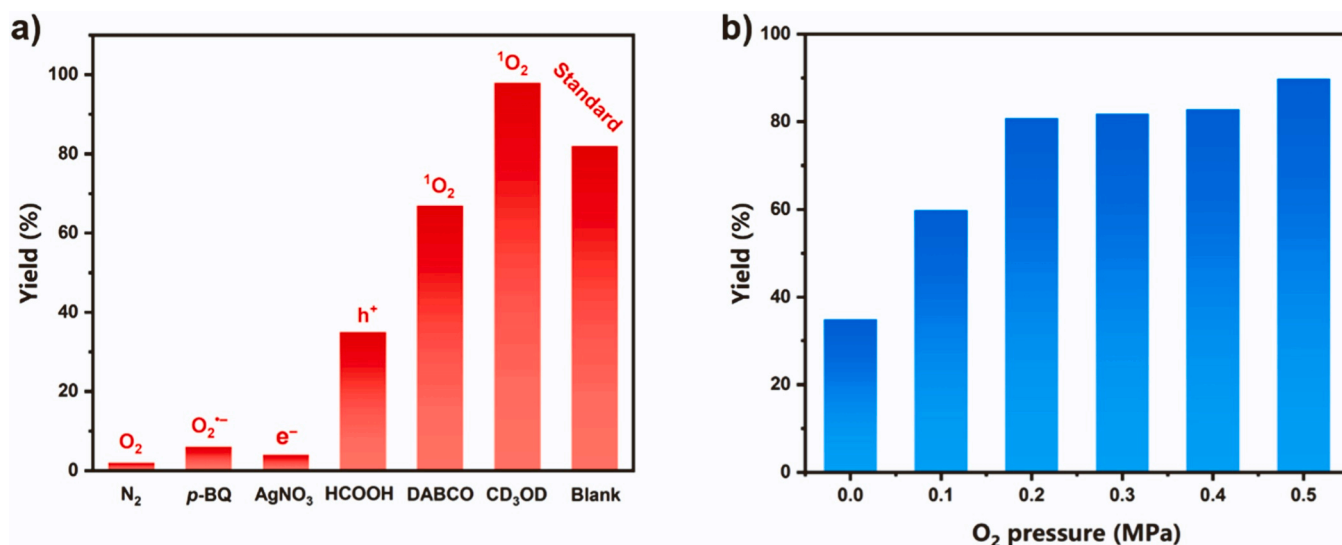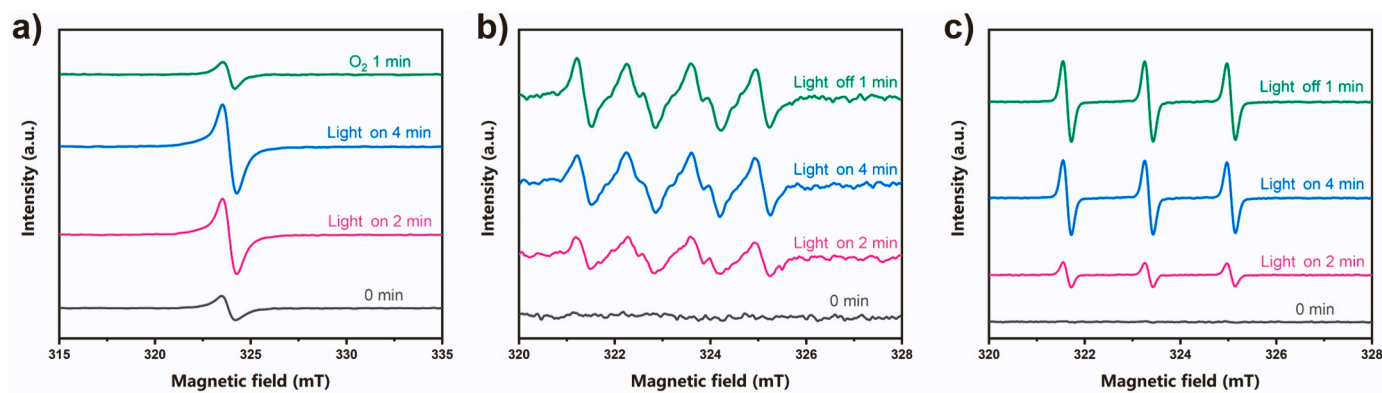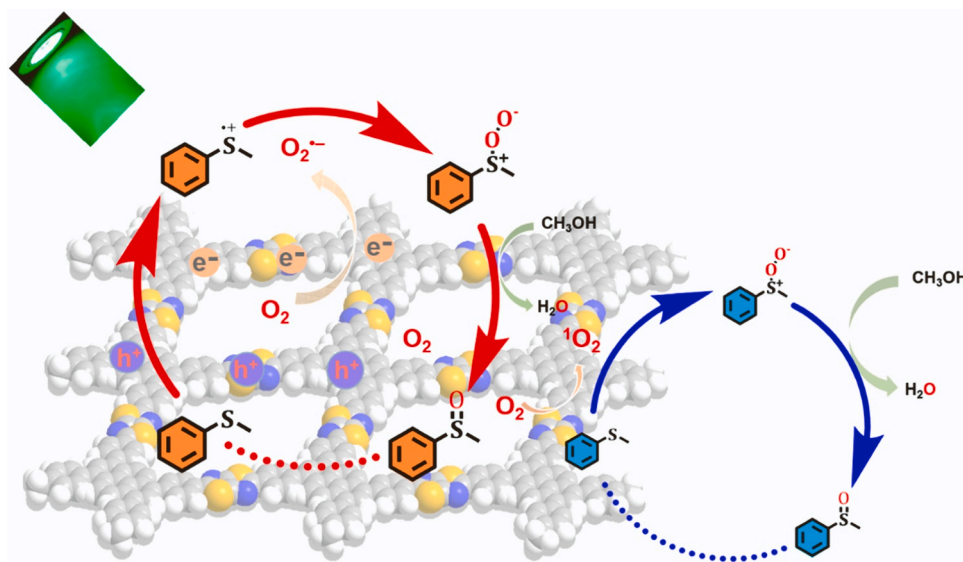

Scheme 2. A plausible mechanism of Py(4)-TzTz-CMP photocatalysis for the green light-promoted oxygenation of thioanisole with O_2.

characterizing the reused Py(4)-TzTz-CMP by PXRD, FTIR, and UV–Vis DRS (Supplementary Fig. S7).

3.3. Mechanistic explorations

After ascertaining the superiority of Py(4)-TzTz-CMP, the photocatalytic selective oxygenation of sulfides with O_2 was further explored to elucidate the reaction mechanism. Generally, ROS are of great importance in photocatalytic oxidations with O_2 [54–63]. Hence, to determine the specific ROS, a suite of quenching experiments was carried out during the green light-promoted oxygenation of thioanisole (Fig. 9a). First, by replacing O_2 with N_2, the reaction did not take place, illustrating O_2 is the prerequisite for the formation of ROS. Next, when the oxygenation of thioanisole using atmospheric O_2 as the oxidant, a much lower conversion (30%) of thioanisole was obtained. Further, the enhancement of O_2 pressure could boost the reaction rate was revealed by a series of O_2 pressure experiments (Fig. 9b). Subsequently, *p*-benzoquinone (*p*-BQ) and silver nitrate (AgNO$_3$) was respectively employed as $O_2^{\bullet-}$ scavenger and electron (e^-) scavenger in this system, and the results indicated that the transformation of thioanisole was observably inhibited, demonstrating that $O_2^{\bullet-}$ is the dominant ROS in the oxidation process. Next, 1,4-diazabicyclo[2.2.2]octane (DABCO) was used as a scavenger of $^1O_2$, and the mild decrease of the yield of product indicated that $^1O_2$ also participated in the formation of methyl phenyl sulfoxide. Further, CD$_3$OD, which could prolong the lifetime of $^1O_2$, was used as

the solvent to check the influence of $^1O_2$. Fascinatingly, the conversion of thioanisole was also enhanced to some extent, which further makes this finding more convincing. Afterward, formic acid (HCOOH) was used as the scavenger of hole (h^+) and the obvious decline in the yield of methyl phenyl sulfoxide was found, suggesting the key role of h^+ in the photocatalytic oxygenation of thioanisole. Based on the above analysis, one can conclude that two types of reaction pathways are responsible for the photocatalytic selective oxygenation of sulfides with O_2, in which the electron transfer pathway is the dominant one.

Further, the LUMO e^-, $O_2^{\bullet-}$ as well as $^1O_2$ were all inspected by in situ electron paramagnetic resonance (EPR) spectroscopy. As shown in Fig. 10a, the photogenerated charge separation and transfer behaviors were captured. The e^- signal was continuously strengthened under the irradiation of green LEDs and then faded sharply after injecting O_2, illustrating that the photogenerated e^- were produced and continually accumulated in Py(4)-TzTz-CMP and then transferred to O_2 to produce ROS. Afterward, the signal of $O_2^{\bullet-}$ was observed by adding the 5,5-dimethyl-1-pyrroline-*N*-oxide (DMPO) as the spin trap of $O_2^{\bullet-}$ (Fig. 10b). In addition, the strong signals of $^1O_2$ engendered by the energy transfer was detected using 2,2,6,6-tetramethyl-4-piperidone (TMPD) as the spin trap in the photocatalytic oxygenation system (Fig. 10c).

Eventually, a plausible mechanism of Py(4)-TzTz-CMP photocatalysis for the green light-promoted oxygenation of thioanisole with O_2 is presented in Scheme 2. First, the e^-–h^+ pair separation of Py(4)-TzTz-CMP is promoted by green light. In the electron transfer

pathway, the e⁻ jump from HOMO to LUMO of the Py(4)-TzTz-CMP photocatalyst and then combines with O_2 to form $O_2^{\bullet-}$. Meanwhile, the photogenerated h⁺ left in the HOMO oxidizes the adsorbed thioanisole to the corresponding sulfur radical cation, which then consumes $O_2^{\bullet-}$ to produce the persulfoxide species. Finally, methyl phenyl sulfoxide is efficiently acquired from persulfoxide with the aid of the solvent CH_3OH. On the other hand, the recombination of excitions could convert O_2 into $^1O_2$ in the energy transfer pathway. Then, $^1O_2$ directly transforms the adjacent thioanisole to a persulfoxide. Similarly, methyl phenyl sulfoxide is obtained aided by the solvent CH_3OH.

4. Conclusions

To summarize, two CMPs based on pyrene with the linkages of TzTz have been prepared for the selective oxygenation of sulfides with O_2. Py(4)-TzTz-CMP and Py(2)-TzTz-CMP were prepared with the molecular building block's symmetries of D_{2h} and C_2, respectively. Importantly, the molecular building block's symmetry directly affected the specific surface areas and π-conjugations of CMPs, endowing a significant impact on their optoelectronic property and the subsequent photocatalytic activity. The dimension of the molecular building block's symmetry on the photocatalytic activity was systematically investigated and subsequently established. Py(4)-TzTz-CMP gave rise to a better photocatalytic activity than Py(2)-TzTz-CMP for the green light-promoted selective oxygenation of organic sulfides with O_2. Intriguingly, both electron and energy transfers were responsible for the production of the targeted sulfoxides. This work offers an innovative platform for selective aerobic oxygenation reactions and gives insight into the rational design of highly active CMPs for photocatalysis.

CRediT authorship contribution statement

Xia Li: Conceptualization, Investigation, Formal analysis, Writing – original draft; **Yuexin Wang**: Investigation, Formal analysis; **Fulin Zhang**: Investigation, Formal analysis; **Xianjun Lang**: Conceptualization, Supervision, Writing – review & editing and Funding acquisition.

Declaration of Competing Interest

The authors declare that they have no known competing financial interests or personal relationships that could have appeared to influence the work reported in this paper.

Data availability

Data will be made available on request.

Acknowledgements

Appendix A. Supporting information

Supplementary data associated with this article can be found in the online version at doi:10.1016/j.apcatb.2023.123190.

References

[1] T. Banerjee, F. Podjaski, J. Kröger, B.P. Biswal, B.V. Lotsch, Polymer photocatalysts for solar-to-chemical energy conversion, Nat. Rev. Mater. 6 (2021) 168–190, https://doi.org/10.1038/s41578-020-00254-z.

[2] S.L. Qiao, M.Y. Di, J.X. Jiang, B.H. Han, Conjugated porous polymers for photocatalysis: The road from catalytic mechanism, molecular structure to advanced applications, Energy Chem 4 (2022), 100094, https://doi.org/10.1016/j.enchem.2022.100094.

[3] C.H. Dai, B. Liu, Conjugated polymers for visible-light-driven photocatalysis, Energy Environ. Sci. 13 (2020) 24–52, https://doi.org/10.1039/c9ee01935a.

[4] S.H. Luo, Z.T. Zeng, G.M. Zeng, Z.F. Liu, R. Xiao, P. Xu, H. Wang, D.L. Huang, Y. Liu, B.B. Shao, Q.H. Liang, D.B. Wang, Q.Y. He, L. Qin, Y.K. Fu, Recent advances in conjugated microporous polymers for photocatalysis: Designs, applications, and prospects, J. Mater. Chem. A 8 (2020) 6434–6470, https://doi.org/10.1039/d0ta01102a.

[5] T. Zhang, G.L. Xing, W.B. Chen, L. Chen, Porous organic polymers: A promising platform for efficient photocatalysis, Mater. Chem. Front. 4 (2020) 332–353, https://doi.org/10.1039/c9qm00633h.

[6] T.X. Wang, H.P. Liang, D.A. Anito, X.S. Ding, B.H. Han, Emerging applications of porous organic polymers in visible-light photocatalysis, J. Mater. Chem. A 8 (2020) 7003–7034, https://doi.org/10.1039/d0ta00364f.

[7] Y.H. Xu, S.B. Jin, H. Xu, A. Nagai, D.L. Jiang, Conjugated microporous polymers: Design, synthesis and application, Chem. Soc. Rev. 42 (2013) 8012–8031, https://doi.org/10.1039/c3cs60160a.

[8] J.S.M. Lee, A.I. Cooper, Advances in conjugated microporous polymers, Chem. Rev. 120 (2020) 2171–2214, https://doi.org/10.1021/acs.chemrev.9b00399.

[9] C.X. Zhao, Z.P. Chen, R. Shi, X.F. Yang, T.R. Zhang, Recent advances in conjugated polymers for visible-light-driven water splitting, Adv. Mater. 32 (2020) 1907296, https://doi.org/10.1002/adma.201907296.

[10] J. Xiao, X.L. Liu, L. Pan, C.X. Shi, X.W. Zhang, J.J. Zou, Heterogeneous photocatalytic organic transformation reactions using conjugated polymers-based materials, ACS Catal. 10 (2020) 12256–12283, https://doi.org/10.1021/acscatal.0c03480.

[11] Y.F. Xu, N. Mao, C. Zhang, X. Wang, J.H. Zeng, Y. Chen, F. Wang, J.X. Jiang, Rational design of donor-π-acceptor conjugated microporous polymers for photocatalytic hydrogen production, Appl. Catal. B: Environ. 228 (2018) 1–9, https://doi.org/10.1016/j.apcatb.2018.01.073.

[12] G.Q. Zhang, W. Ou, J. Wang, Y.S. Xu, D. Xu, T. Sun, S.N. Xiao, M.R. Wang, H.X. Li, W. Chen, C.L. Su, Stable, carrier separation tailorable conjugated microporous polymers as a platform for highly efficient photocatalytic H₂ evolution, Appl. Catal. B: Environ. 245 (2019) 114–121, https://doi.org/10.1016/j.apcatb.2018.12.007.

[13] Z.L. Li, H. Fang, Z.P. Chen, W.X. Zou, C.X. Zhao, X.F. Yang, Regulating donor-acceptor interactions in triazine-based conjugated polymers for boosted photocatalytic hydrogen production, Appl. Catal. B: Environ. 312 (2022) 121374, https://doi.org/10.1016/j.apcatb.2022.121374.

[14] Z.J. Wang, X.Y. Yang, T.J. Yang, Y.B. Zhao, F. Wang, Y. Chen, J.H. Zeng, C. Yan, F. Huang, J.X. Jiang, Dibenzothiophene dioxide based conjugated microporous polymers for visible-light-driven hydrogen production, ACS Catal. 8 (2018) 8590–8596, https://doi.org/10.1021/acscatal.8b02607.

[15] A.M. Elewa, A.F.M. El-Mahdy, M.H. Elsayed, M.G. Mohamed, S.W. Kuo, H.H. Chou, Sulfur-doped triazine-conjugated microporous polymers for achieving the robust visible-light-driven hydrogen evolution, Chem. Eng. J. 421 (2021) 129825, https://doi.org/10.1016/j.cej.2021.129825.

[16] A.F. Saber, A.M. Elewa, H.H. Chou, A.F.M. El-Mahdy, Donor-acceptor carbazole-based conjugated microporous polymers as photocatalysts for visible-light-driven H₂ and O₂ evolution from water splitting, Appl. Catal. B: Environ. 316 (2022) 121624, https://doi.org/10.1016/j.apcatb.2022.121624.

[17] W.L. Zhao, D. Zhai, C.C. Liu, D.Y. Zheng, H. Wu, L. Sun, Z. Li, T. Yu, W. Zhou, X. Fang, S.L. Zhai, K.L. Han, Z.L. He, W.Q. Deng, Unblocked intramolecular charge transfer for enhanced CO₂ photoreduction enabled by an imidazolium-based ionic conjugated microporous polymer, Appl. Catal. B: Environ. 300 (2022) 120719, https://doi.org/10.1016/j.apcatb.2021.120719.

[18] Y.C. Wang, H. Liu, Q.Y. Pan, N.X. Ding, C.M. Yang, Z.H. Zhang, C.C. Jia, Z.B. Li, J. Liu, Y.J. Zhao, Construction of thiazolo[5,4-d]thiazole-based two-dimensional network for efficient photocatalytic CO₂ reduction, ACS Appl. Mater. Interfaces 12 (2020) 46483–46489, https://doi.org/10.1021/acsami.0c12173.

[19] S. Barman, A. Singh, F.A. Rahimi, T.K. Maji, Metal-free catalysis: A redox-active donor–acceptor conjugated microporous polymer for selective visible-light-driven CO₂ reduction to CH₄, J. Am. Chem. Soc. 143 (2021) 16284–16292, https://doi.org/10.1021/jacs.1c07916.

[20] X.Y. Huang, Y.L. Lu, G.J. Mao, S.H. Yin, B. Long, G.J. Deng, A. Ali, T. Song, Polarization engineering of porous organic polymers for superior photocatalytic synthesis of disulfides and CO₂ reduction, J. Mater. Chem. A 10 (2022) 24147–24155, https://doi.org/10.1039/d2ta06941e.

[21] Y.S. Li, M.X. Liu, L. Chen, Polyoxometalate built-in conjugated microporous polymers for visible-light heterogeneous photocatalysis, J. Mater. Chem. A 5 (2017) 13757–13762, https://doi.org/10.1039/c7ta03776g.

[22] J. Chakraborty, I. Nath, C. Jabbour, N. Aljammal, S.X. Song, C.M. Kao, P. M. Heynderickx, F. Verpoort, Novel rapid room temperature synthesis of conjugated microporous polymer for metal-free photocatalytic degradation of fluoroquinolones, J. Hazard. Mater. 398 (2020), 122928, https://doi.org/10.1016/j.jhazmat.2020.122928.

[23] C. Xu, Q.J. Xie, W.J. Zhang, S.H. Xiong, C.Y. Pan, J.T. Tang, G.P. Yu, A vinylene-bridged conjugated covalent triazine polymer as a visible-light-active photocatalyst for degradation of methylene blue, Macromol. Rapid Commun. 41 (2020) 2000006, https://doi.org/10.1002/marc.202000006.

[24] X.Y. Dong, H.M. Hao, F.L. Zhang, X.J. Lang, Blue light photocatalysis of carbazole-based conjugated microporous polymers: Aerobic hydroxylation of phenylboronic acids to phenols, Appl. Catal. B: Environ. (2022), 121210, https://doi.org/10.1016/j.apcatb.2022.121210.

[25] Y.F. Zhi, Z.J. Yao, W.B. Jiang, H. Xia, Z. Shi, Y. Mu, X.M. Liu, Conjugated microporous polymers as heterogeneous photocatalysts for efficient degradation of

a mustard-gas simulant, ACS Appl. Mater. Interfaces 11 (2019) 37578–37585, https://doi.org/10.1021/acsami.9b10958.

[26] W.T. Gong, K.X. Dong, L. Liu, M. Hassan, G.L. Ning, β-Diketone boron difluoride dye-functionalized conjugated microporous polymers for efficient aerobic oxidative photocatalysis, Catal. Sci. Technol. 11 (2021) 3905–3913, https://doi.org/10.1039/d1cy00384d.

[27] S.Z. Li, W.J. Zhang, S. Yang, F. Chen, C.Y. Pan, J.T. Tang, K.A.I. Zhang, G.P. Yu, Phenothiazine-based conjugated microporous polymers: Pore surface and bandgap engineering for visible light-driven aerobic oxidative cyanation, Chem. Eng. J. 408 (2021), 127261, https://doi.org/10.1016/j.cej.2020.127261.

[28] W. Ou, G.Q. Zhang, J. Wu, C.L. Su, Photocatalytic cascade radical cyclization approach to bioactive indoline-alkaloids over donor–acceptor type conjugated microporous polymer, ACS Catal. 9 (2019) 5178–5183, https://doi.org/10.1021/acscatal.9b00693.

[29] Q.J. Xie, Y.M. Yang, W.J. Zhang, Z. Gao, X.F. Li, J.T. Tang, C.Y. Pan, G.P. Yu, Polarization-induced charge separation in conjugated microporous polymers for efficient visible light-driven C-3 selenocyanation of indoles, Chem. Sci. 12 (2021) 5631–5637, https://doi.org/10.1039/d0sc06951e.

[30] V. Srivastava, P.K. Singh, P.P. Singh, Recent advances of visible-light photocatalysis in the functionalization of organic compounds, J. Photochem. Photobiol., C. 50 (2022), 100488, https://doi.org/10.1016/j.jphotochemrev.2022.100488.

[31] C.H. Han, R.J. Qi, R.L. Sun, K.C. Fan, B. Johannessen, D.C. Qi, S.W. Cao, J.S. Xu, Enhanced support effects in single-atom copper-incorporated carbon nitride for photocatalytic Suzuki cross-coupling reactions, Appl. Catal. B: Environ. 320 (2023), 121954, https://doi.org/10.1016/j.apcatb.2022.121954.

[32] Z.R. Wang, C. Zhu, Z.T. Ni, H. Hojo, H. Einaga, Enhanced photocatalytic benzene oxidation to phenol over monoclinic WO$_3$ nanorods under visible light, ACS Catal. 12 (2022) 14976–14989, https://doi.org/10.1021/acscatal.2c03832.

[33] X.L. Liu, D.J. Dai, Z.H. Cui, Q.Q. Zhang, X.Q. Gong, Z.Y. Wang, Y.Y. Liu, Z. K. Zheng, H.F. Cheng, Y. Dai, B.B. Huang, P. Wang, Optimizing the reaction pathway by active site regulation in the CdS/Fe$_2$O$_3$ Z-scheme heterojunction system for highly selective photocatalytic benzylamine oxidation integrated with H$_2$ production, ACS Catal. 12 (2022) 12386–12397, https://doi.org/10.1021/acscatal.2c03550.

[34] S. Wei, H.X. Zhong, H.T. Wang, Y.J. Song, C.M. Jia, M. Anpo, L. Wu, Oxygen vacancy enhanced visible light photocatalytic selective oxidation of benzylamine over ultrathin Pd/BiOCl nanosheets, Appl. Catal. B: Environ. 305 (2022), 121032, https://doi.org/10.1016/j.apcatb.2021.121032.

[35] R.Q. Zhang, Y.Y. Liu, Z.Y. Wang, P. Wang, Z.K. Zheng, X.Y. Qin, X.Y. Zhang, Y. Dai, M.H. Whangbo, B.B. Huang, Selective photocatalytic conversion of alcohol to aldehydes by singlet oxygen over Bi-based metal-organic frameworks under UV–vis light irradiation, Appl. Catal. B: Environ. 254 (2019) 463–470, https://doi.org/10.1016/j.apcatb.2019.05.024.

[36] Z.W. Zhang, J. Jia, Y.F. Zhi, S. Ma, X.M. Liu, Porous organic polymers for light-driven organic transformations, Chem. Soc. Rev. 51 (2022) 2444–2490, https://doi.org/10.1039/d1cs00808k.

[37] C.L. Su, R. Tandiana, B.B. Tian, A. Sengupta, W. Tang, J. Su, K.P. Loh, Visible-light photocatalysis of aerobic oxidation reactions using carbazolic conjugated microporous polymers, ACS Catal. 6 (2016) 3594–3599, https://doi.org/10.1021/acscatal.6b00443.

[38] Y.F. Zhi, S. Ma, H. Xia, Y.M. Zhang, Z. Shi, Y. Mu, X.M. Liu, Construction of donor-acceptor type conjugated microporous polymers: A fascinating strategy for the development of efficient heterogeneous photocatalysts in organic synthesis, Appl. Catal. B: Environ. 244 (2019) 36–44, https://doi.org/10.1016/j.apcatb.2018.11.032.

[39] V.R. Battula, H. Singh, S. Kumar, I. Bala, S.K. Pal, K. Kailasam, Natural sunlight driven oxidative homocoupling of amines by a truxene-based conjugated microporous polymer, ACS Catal. 8 (2018) 6751–6759, https://doi.org/10.1021/acscatal.8b00623.

[40] X.M. Gao, C. Shu, C. Zhang, W.Y. Ma, S.B. Ren, F. Wang, Y. Chen, J.H. Zeng, J. X. Jiang, Substituent effect of conjugated microporous polymers on the photocatalytic hydrogen evolution activity, J. Mater. Chem. A 8 (2020) 2404–2411, https://doi.org/10.1039/c9ta13212k.

[41] S.Y. Wang, X. Hai, X. Ding, S.B. Jin, Y.G. Xiang, P. Wang, B. Jiang, F. Ichihara, M. Oshikiri, X.G. Meng, Y.X. Li, W. Matsuda, J. Ma, S. Seki, X.P. Wang, H. Huang, Y. Wada, H. Chen, J.H. Ye, Intermolecular cascaded π-conjugation channels for electron delivery powering CO$_2$ photoreduction, Nat. Commun. 11 (2020) 1149, https://doi.org/10.1038/s41467-020-14851-7.

[42] X. Li, F.L. Zhang, Y.X. Wang, K.H. Xiong, X.J. Lang, Extending the 2D conjugated microporous polymers linked by thiazolo[5,4-*d*]thiazole for green light-driven selective aerobic oxidation of amines, J. Mater. Chem. A 10 (2022) 14965–14975, https://doi.org/10.1039/d2ta02603a.

[43] W.H. Sun, Y.G. Xiang, Z.H. Jiang, S.Y. Wang, N. Yang, S.B. Jin, L.H. Sun, H.L. Teng, H. Chen, Designed polymeric conjugation motivates tunable activation of

molecular oxygen in heterogeneous organic photosynthesis, Sci. Bull. 67 (2022) 61–70, https://doi.org/10.1016/j.scib.2021.07.016.

[44] X.Y. Dong, F.L. Zhang, F.W. Huang, X.J. Lang, Pyrene-based conjugated microporous polymers for red light-powered oxidation of amines to imines, Appl. Catal. B: Environ. 318 (2022), 121875, https://doi.org/10.1016/j.apcatb.2022.121875.

[45] W.L. Sheng, X.X. Wang, Y.X. Wang, S.L. Chen, X.J. Lang, Integrating TEMPO into a metal–organic framework for cooperative photocatalysis: Selective aerobic oxidation of sulfides, ACS Catal. 12 (2022) 11078–11088, https://doi.org/10.1021/acscatal.2c02519.

[46] C.J. Wu, X.Y. Li, T.R. Li, M.Z. Shao, L.J. Niu, X.F. Lu, J.L. Kan, Y. Geng, Y.B. Dong, Natural sunlight photocatalytic synthesis of benzoxazole-bridged covalent organic framework for photocatalysis, J. Am. Chem. Soc. 144 (2022) 18750–18755, https://doi.org/10.1021/jacs.2c07893.

[47] D. Chen, W.B. Chen, G. Zhang, S. Li, W.H. Chen, G.L. Xing, L. Chen, N-rich 2D heptazine covalent organic frameworks as efficient metal-free photocatalysts, ACS Catal. 12 (2022) 616–623, https://doi.org/10.1021/acscatal.1c05233.

[48] Z.P. Xie, W.B. Wang, X.T. Ke, X. Cai, X. Chen, S.B. Wang, W. Lin, X.C. Wang, A heptazine-based polymer photocatalyst with donor-acceptor configuration to promote exciton dissociation and charge separation, Appl. Catal. B: Environ. 325 (2023), 122312, https://doi.org/10.1016/j.apcatb.2022.122312.

[49] H. Li, X. Li, J. Zhou, W.L. Sheng, X.J. Lang, Extending aromatic acids on TiO$_2$ for cooperative photocatalysis with triethylamine: Violet light-induced selective aerobic oxidation of sulfides, Chin. Chem. Lett. 33 (2022) 3733–3738, https://doi.org/10.1016/j.cclet.2021.10.068.

[50] C.G. López-Calixto, S. Cabrera, R. Pérez-Ruiz, M. Barawi, J. Alemán, V.A. de la Peña O'Shea, M. Liras, Conjugated porous polymer based on BOPHY dyes as photocatalyst under visible light, Appl. Catal. B: Environ. 258 (2019), 117933, https://doi.org/10.1016/j.apcatb.2019.117933.

[51] S. Guo, L.H. Kong, P. Wang, S. Yao, T.B. Lu, Z.M. Zhang, Switching excited state distribution of metal–organic framework for dramatically boosting photocatalysis, Angew. Chem. Int. Ed. 61 (2022), e202206193, https://doi.org/10.1002/anie.202206193.

[52] Y.Y. Qan, D.D. Li, Y.L. Han, H.L. Jiang, Photocatalytic molecular oxygen activation by regulating excitonic effects in covalent organic frameworks, J. Am. Chem. Soc. 142 (2020) 20763–20771, https://doi.org/10.1021/jacs.0c09727.

[53] Y. Kondo, K. Hino, Y. Kuwahara, K. Mori, H. Yamashita, Photosynthesis of hydrogen peroxide from dioxygen and water using aluminium-based metal–organic framework assembled with porphyrin- and pyrene-based linkers, J. Mater. Chem. A 11 (2023) 9530–9537, https://doi.org/10.1039/d3ta01051a.

[54] Y.L. Wen, J.W. Yan, B.X. Yang, Z.Y. Zhuang, Y. Yu, Reactive oxygen species on transition metal-based catalysts for sustainable environmental applications, J. Mater. Chem. A 10 (2022) 19184–19210, https://doi.org/10.1039/d2ta02188a.

[55] L. Luo, T.T. Zhang, M. Wang, R.P. Yun, X. Xiang, Recent advances in heterogeneous photo-driven oxidation of organic molecules by reactive oxygen species, ChemSusChem 13 (2020) 5173–5184, https://doi.org/10.1002/cssc.202001398.

[56] L.L. Wang, X. Lan, W.Y. Peng, Z.H. Wang, Uncertainty and misinterpretation over identification, quantification and transformation of reactive species generated in catalytic oxidation processes: A review, J. Hazard. Mater. 408 (2021), 124436, https://doi.org/10.1016/j.jhazmat.2020.124436.

[57] Y.Z. Chen, Z.U. Wang, H.W. Wang, J.L. Lu, S.H. Yu, H.L. Jiang, Singlet oxygen-engaged selective photo-oxidation over Pt nanocrystals/porphyrinic MOF: The roles of photothermal effect and Pt electronic state, J. Am. Chem. Soc. 139 (2017) 2035–2044, https://doi.org/10.1021/jacs.6b12074.

[58] S. Li, L. Dai, L. Li, A.W. Dong, J.N. Li, X.J. Meng, B. Wang, P.F. Li, Post-oxidation of a fully conjugated benzotrithiophene-based COF for photocatalytic detoxification of a sulfur mustard simulant, J. Mater. Chem. A 10 (2022) 13325–13332, https://doi.org/10.1039/d2ta01864k.

[59] Y. Chen, M.J. Xu, J.Y. Wen, Y. Wan, Q.F. Zhao, X. Cao, Y. Ding, Z.L. Wang, H.X. Li, Z.F. Bian, Selective recovery of precious metals through photocatalysis, Nat. Sustainability 4 (2021) 618–626, https://doi.org/10.1038/s41893-021-00697-4.

[60] Y.Z. Peng, G.C. Guo, S. Guo, L.H. Kong, T.B. Lu, Z.M. Zhang, Charge transfer from donor to acceptor in conjugated microporous polymer for enhanced photosensitization, Angew. Chem. Int. Ed. 60 (2021) 22062–22069, https://doi.org/10.1002/anie.202109968.

[61] Y. Kondo, Y. Kuwahara, K. Mori, H. Yamashita, Design of metal-organic framework catalysts for photocatalytic hydrogen peroxide production, Chem 8 (2022) 2924–2938, https://doi.org/10.1016/j.chempr.2022.10.007.

[62] Q.X. Zhang, Z.P. Zhang, D.Y. Zhao, L. Wang, H. Li, F. Zhang, Y.N. Huo, H.X. Li, Synergistic photocatalytic-photothermal contribution enhanced by recovered Ag$^+$ ions on MXene membrane for organic pollutant removal, Appl. Catal. B: Environ. 320 (2023), 122009, https://doi.org/10.1016/j.apcatb.2022.122009.

[63] C. Yang, R. Li, K.A.I. Zhang, W. Lin, K. Landfester, X.C. Wang, Heterogeneous photoredox flow chemistry for the scalable organosynthesis of fine chemicals, Nat. Commun. 11 (2020) 1239, https://doi.org/10.1038/s41467-020-14983-w.